INTERNATIONAL JOURNAL FOR NUMERICAL METHODS IN FLUIDS, VOL. 18, 605–625 (1994)

A VERTEX-CENTRED FINITE VOLUME METHOD WITH SHOCK DETECTION

P. I. CRUMPTON AND G. J. SHAW

Oxford University Computing Laboratory, Numerical Analysis Group, 11 Keble Road, Oxford OX1 3QD, U.K.

SUMMARY

This paper introduces a vertex-centred finite volume method for compressible viscous flow incorporating a new shock detection procedure. The discretization is designed to be robust and accurate on the highly stretched and curved meshes necessary for resolving turbulent boundary layers around the leading edge of an aerofoil. Details of the method are described for two-dimensional problems and the natural extension to three-dimensional multiblock meshes is discussed. The shock detection procedure is used to limit the range of the shock-capturing dissipation specifically to regions containing shocks. For transonic turbulent flow this is shown to improve the boundary layer representation significantly.

KEY WORDS Vertex-centred Finite volume Multigrid Navier–Stokes Shock detection Turbulence

1. INTRODUCTION

Vertex-centred finite volume methods have recently been much used for the solution of the compressible Euler and Navier–Stokes equations.[1,2] On a two-dimensional structured mesh the basic methodology is that the conservation laws, by which these equations are represented, are integrated over a control volume whose vertices are the centroids of four neighbouring mesh cells. Unlike the cell vertex method,[3,4] this results in a natural correspondence between equations and unknowns which facilitates the design of iterative solution procedures. However, the potential accuracy of the cell vertex approximation is very attractive; this is not realized in practise because the individual residuals are not set to zero, only a matrix-weighted average. In order for comparison, cell vertex results of the same test problems presented here are available in Reference 5.

For highly stretched meshes with large curvature, which are necessary for the accurate simulation of turbulent boundary layers around an aerofoil, these vertex-centred methods suffer certain disadvantages. The most significant of these is that a given nodal unknown is not always located within the control volume which updates it. Furthermore, the union of control volumes may differ substantially from the region on which a solution is required.[6]

This paper presents a modified vertex-centred scheme which is designed to rectify the disadvantages mentioned above. The control volume for this method is an octagon whose vertices are centroids and mid-side points of neighbouring mesh cells. Inviscid, viscous and artificial terms are all discretized consistently over this volume. This approach readily extends to multiblock grids and unstructured triangular meshes, for which similar methods have been used in Reference 7. The resulting algebraic system is solved efficiently using multigrid.[8]

In addition, the paper introduces a new shock detection algorithm which is used to limit the range of application of shock-capturing artificial viscosity specifically to those regions where it

CCC 0271–2091/94/060605–21

Received April 1993
Revised November 1993

is required. Conventionally, artificial viscosity is typically controlled according to the magnitude of the pressure curvature,[9] which may lead to unnecessarily large amounts of artificial damping in boundary layers. For transonic turbulent flow the approach adopted here is shown to improve the boundary layer representation significantly.

The paper begins with a description of the vertex-centred finite volume scheme. The discretization of inviscid, viscous and artificial diffusion terms is described in detail. In addition, the treatment of boundary conditions, including interior multiblock boundaries, is discussed. Section 3 presents a brief account of the multigrid solution procedure used to solve the discrete non-linear algebraic system. In Section 4 the shock detection algorithm is derived and discussed. Section 5 is devoted to a Fourier analysis of the two vertex-centred scheme discussed here. Finally, Section 6 presents numerical results for laminar flow past an NACA 0012 aerofoil and for turbulent flow past an RAE 2822 aerofoil.

2. THE FINITE VOLUME DISCRETIZATION

This paper addresses the numerical solution of systems of conservation laws of the general form

$$\nabla \cdot \mathscr{F} = 0, \qquad \mathscr{F} = (\mathbf{f}, \mathbf{g}), \tag{1}$$

where

$$\mathbf{f} = \mathbf{f}(\mathbf{w}, \nabla \mathbf{w}), \qquad \mathbf{g} = \mathbf{g}(\mathbf{w}, \nabla \mathbf{w}), \tag{2}$$

$$\mathbf{w} = \mathbf{w}(\mathbf{x}), \quad \mathbf{x} \in \Omega \subset \mathbb{R}^2, \tag{3}$$

for some open domain Ω. Note that the fluxes for this general form are functions not only of $\mathbf{w}$ but also of its gradient. For convenience the fluxes can be written as

$$(\mathbf{f}, \mathbf{g}) = (\mathbf{f}^{\mathrm{I}}(\mathbf{w}), \mathbf{g}^{\mathrm{I}}(\mathbf{w})) + (\mathbf{f}^{\mathrm{V}}(\mathbf{w}, \nabla \mathbf{w}), \mathbf{g}^{\mathrm{V}}(\mathbf{w}, \nabla \mathbf{w})) \tag{4}$$

where $(\mathbf{f}^{\mathrm{I}}, \mathbf{g}^{\mathrm{I}})$ and $(\mathbf{f}^{\mathrm{V}}, \mathbf{g}^{\mathrm{V}})$ represent the inviscid and viscous fluxes respectively. Of particular interest in this paper are the steady compressible Reynolds-averaged Navier–Stokes equation in two dimensions, $\mathbf{x} = (x, y)$, for which

$$\mathbf{w} = \begin{pmatrix} \rho \\ \rho u \\ \rho v \\ E \end{pmatrix}, \qquad \mathbf{f}^{\mathrm{I}} = \begin{pmatrix} \rho u \\ \rho u^2 + p \\ \rho uv \\ u(E + p) \end{pmatrix}, \qquad \mathbf{g}^{\mathrm{I}} = \begin{pmatrix} \rho u \\ \rho uv \\ \rho v^2 + p \\ v(E + p) \end{pmatrix}, \tag{5}$$

$$\mathbf{f}^{\mathrm{V}} = \begin{pmatrix} 0 \\ -\tau_{xx} \\ -\tau_{xy} \\ -u\tau_{xx} - v\tau_{xy} + q_x \end{pmatrix}, \qquad \mathbf{g}^{\mathrm{V}} = \begin{pmatrix} 0 \\ -\tau_{xy} \\ -\tau_{yy} \\ -u\tau_{xy} - v\tau_{yy} + q_y \end{pmatrix}, \tag{6}$$

where ρ, u, v, p and E denote the density, the two Cartesian components of velocity, the pressure and the total energy respectively. The fluid is assumed to be a perfect gas, for which the equation of state is

$$p = (\gamma - 1)[E - \tfrac{1}{2}\rho(u^2 + v^2)], \tag{7}$$

with the speed of sound c given by $c^2 = \gamma p/\rho$, the enthalpy $H = (E + p)/\rho$ and the entropy $S = p/\rho^\gamma$. The deviatoric stress and heat conduction terms are given by

$$\tau_{xx} = \frac{2(\mu_l + \mu_t)}{3Re}\left(2\frac{\partial u}{\partial x} - \frac{\partial v}{\partial y}\right), \tag{8}$$

$$\tau_{xy} = \frac{\mu_l + \mu_t}{Re}\left(\frac{\partial u}{\partial y} + \frac{\partial v}{\partial x}\right), \tag{9}$$

$$\tau_{yy} = \frac{2(\mu_l + \mu_t)}{3Re}\left(2\frac{\partial v}{\partial y} - \frac{\partial u}{\partial x}\right), \tag{10}$$

$$q_x = -\left(\frac{\mu_l}{Pr} + \frac{\mu_t}{Pr_t}\right)\frac{1}{(\gamma - 1)M_\infty^2 Re}\frac{\partial T}{\partial x}, \tag{11}$$

$$q_y = -\left(\frac{\mu_l}{Pr} + \frac{\mu_t}{Pr_t}\right)\frac{1}{(\gamma - 1)M_\infty^2 Re}\frac{\partial T}{\partial y}, \tag{12}$$

where γ, κ, Re, Pr and M_∞ denote the adiabatic constant, the coefficient of thermal conductivity, the Reynolds number, the Prandtl number and the freestream Mach number respectively. The laminar viscosity μ_l is assumed to vary with temperature according to Sutherland's law.[10] The turbulent viscosity μ_t is defined using the model of Baldwin and Lomax[11] with the slight modifications of Reference 12. Pr_t denotes the turbulent Prandtl number.

2.1. *A vertex-centred approach*

It is assumed that a set of non-overlapping convex quadrilaterals which tessellate Ω is given; this will be referred to as the primary mesh. In the vertex-centred methodology the unknowns are stored at the vertices $\{\mathbf{x}_j : j = 1, 2, \ldots, N\}$ of the primary mesh and a control volume Ω_j with boundary $\delta\Omega_j$ is constructed around each vertex $\mathbf{x}_j$.

Definining the residuals

$$\mathbf{r}_j(\mathbf{w}) = \frac{1}{c_j}\oint_{\delta\Omega_j} \mathscr{F} \cdot \mathbf{n}\, ds, \quad j = 1, 2, \ldots, N, \tag{13}$$

where V_j is the measure of the control volume Ω_j and $\mathbf{n}$ is the outward unit normal to $\delta\Omega_j$, it is clear from the divergence theorem that $\mathbf{r}_j = \mathbf{o}$ if $\mathbf{w}$ is a solution of (1). Finite volume schemes are discrete approximations to $\mathbf{r}_j$ which ensure conservation and convergence to a weak solution of equation (1). These properties are imperative if the solution admits shock waves.[13]

The construction of the control volume Ω_j around the vertex $\mathbf{x}_j$ can be done in many ways. Two alternatives are discussed here. The first[1,2,14] is to define the control volume to the quadrilateral whose vertices are the centroids of the primary mesh cells with common vertex $\mathbf{x}_j$ (Figure 1(a)). An alternative approach is to define the control volume as the octagon whose vertices are the centroids and mid-edge points of the primary mesh cells surrounding $\mathbf{x}_j$ (Figure 1(b)).

The motivation behind the latter approach adopted here is to ensure

(i) that the node $\mathbf{x}_j$ always lies within μ_j
(ii) that the union of control volumes is identical to the union of primary mesh cells.

This robust control volume is thought to be particularly important on the highly stretched

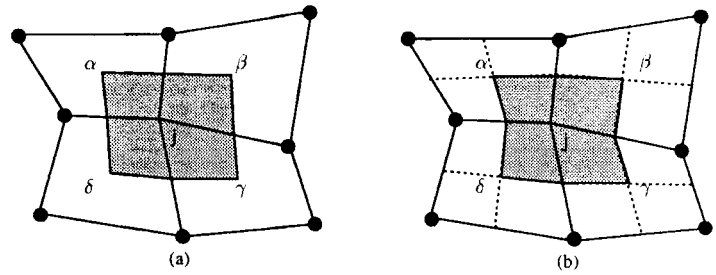

Figure 1. Alternative control volume for vertex $\mathbf{x}_j$ on an irregular mesh

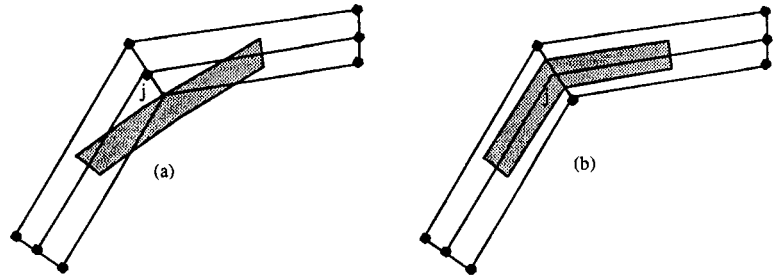

Figure 2. An alternative control volume for vertex $\mathbf{x}_j$ on a stretched curved mesh

and curved meshes necessary for resolving turbulent boundary layers around the leading edge of an aerofoil. Figure 2 exemplifies the alternative approaches on such meshes, showing in particular that the properties listed above do not hold for the method of Reference 2.

In order to construct the approximation to $\mathbf{r}_j$ in equation (13), first define

$$\mathbf{I}_{\alpha,S} \approx \int_{\frac{1}{2}(\mathbf{x}_1+\mathbf{x}_2)}^{\mathbf{x}_0} \mathscr{F} \cdot \mathbf{n}\, ds \tag{14}$$

as an approximation to the line integral of the flux along the southern line of the primary mesh cell α (Figure 3). Similarly define $\mathbf{I}_{\alpha,W}$, $\mathbf{I}_{\alpha,E}$ and $\mathbf{I}_{\alpha,N}$ as the approximate line integrals along the western, eastern and northern lines respectively, integrating from the mid-edge point to the centroid, with an approximate unit normal $\mathbf{n}$ to be defined later. Thus the contribution of the contour integral required for, say, vertex $\mathbf{x}_2$ from the primary mesh cell α in Figure 3 is

$$\mathbf{C}_{\alpha,2} = \mathbf{I}_{\alpha,E} - \mathbf{I}_{\alpha,S} \tag{15}$$

and similarly for $\mathbf{C}_{\alpha,1}$, $\mathbf{C}_{\alpha,3}$ and $\mathbf{C}_{\alpha,4}$. The approximation to the residual equation (13) at a vertex $\mathbf{x}_j$ on the primary mesh can therefore be expressed as

$$\mathbf{R}_j = \frac{1}{V_j} \sum_{\alpha=1}^{p} \mathbf{C}_{\alpha,j}, \tag{16}$$

where the integer $p \geq 4$ represents the possible p cells surrounding vertex x_j. Although in this study body-fitted structured meshes are used, for which $p = 4$, it is envisaged that in general multiblock meshes will be necessary to resolve complex geometrical configurations. In this case

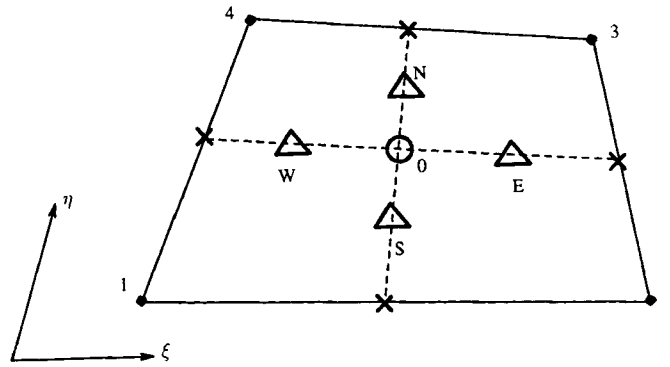

Figure 3. Detail of a primary cell α: ●, vertex on primary mesh; ×, mid-edge point; ○, centroid of cell; △, north, south, east and west points

many primary cells may have a common vertex at multiblock boundaries,[15] leading to $p > 4$. The authors believe it to be important for any discretization on a structured mesh to cope readily with this situation. By expressing the residual as a distribution of integrals based within the primary mesh, as in equation (16), no discretization problems are envisaged at multiblock boundaries.

Figure 3 illustrates in some details a primary cell where the centroid is defined as

$$\mathbf{x}_0 = \tfrac{1}{4} \sum_{i=1}^{4} \mathbf{x}_i, \tag{17}$$

where $\mathbf{x}_i$ are the vertices of the primary cell α. Using a compass point notation, the southern point $\mathbf{x}_S$ lies halfway between $\mathbf{x}_0$ and the mid-edge point between $\mathbf{x}_1$ and $\mathbf{x}_2$. Thus

$$\mathbf{x}_S = \tfrac{1}{8}(3\mathbf{x}_1 + 3\mathbf{x}_2 + \mathbf{x}_3 + \mathbf{x}_4) \tag{18}$$

and similarly for $\mathbf{x}_E$, $\mathbf{x}_W$ and $\mathbf{x}_N$. It is worth noting that

$$\tfrac{1}{2}(\mathbf{x}_4 + \mathbf{x}_3) - \mathbf{x}_0 = \mathbf{x}_0 - \tfrac{1}{2}(\mathbf{x}_1 + \mathbf{x}_2), \tag{19}$$

so both the lengths and normals of the southern and northern lines are identical. This significantly reduces the complexity and work required to compute the line integrals within a primary cell, which is particularly important in three dimensions. It is thus worthwhile defining the primary-cell-based distances and unit normals

$$S_{NS} = \tfrac{1}{4}|\mathbf{x}_3 + \mathbf{x}_4 - \mathbf{x}_1 - \mathbf{x}_2|, \tag{20}$$

$$\mathbf{n}_{NS} = \frac{1}{4S_{NS}}(-(y_3 + y_4 - y_1 - y_2), (x_3 + x_4 - x_1 - x_2))^{\mathrm{T}} \tag{21}$$

and similarly for S_{EW} and $\mathbf{n}_{EW}$.

Numerical approximations to the integrals (16) are defined in terms of the discrete node-based quantities

$$\mathbf{W}_j \approx \mathbf{w}(\mathbf{x}_j), \tag{22}$$

$$\nabla\mathbf{W}_j \approx \nabla\mathbf{w}(\mathbf{x}_j). \tag{23}$$

To evaluate (14), the midpoint rule is used:

$$\mathbf{I}_{\alpha,S} = (\mathbf{F}_S, \mathbf{G}_S)\cdot\mathbf{n}_{NS}S_{NS} + \lambda_{NS}\mathbf{D}_S, \tag{24}$$

where $\mathbf{F}_S \approx \mathbf{f}(\mathbf{w}_S, \nabla\mathbf{w}_S)$, $\mathbf{w}_S = \mathbf{w}(\mathbf{x}_S)$, $\mathbf{D}_S$ is an artificial diffusion operator acting on the discrete solution $\mathbf{W}$ and λ_{NS} is a acalar upwind coefficient. Details of $\mathbf{D}_S$ and λ_{NS} will be given in Section 2.3. The flux $\mathbf{F}_S$ is evaluated in an analogous fashion to $\mathbf{x}_S$ in (18) by

$$\mathbf{F}_S = \tfrac{1}{8}(3\mathbf{F}_1 + 3\mathbf{F}_2 + \mathbf{F}_3 + \mathbf{F}_4), \tag{25}$$

where $\mathbf{F}_j = \mathbf{f}(\mathbf{W}_j, \nabla\mathbf{W}_j)$ for vertex $\mathbf{x}_j$ of the primary mesh. Similarly $\mathbf{I}_{\alpha,N}$, $\mathbf{I}_{\alpha,W}$ and $\mathbf{I}_{\alpha,W}$ can be defined. An alternative to (25) would be to average the states to evaluate $\mathbf{W}_S$ and to derive the flux $\mathbf{F}_S$ from this approximation. However, this would require approximately $4N^2$ computations of $\mathbf{F}$ over an $N \times N$ mesh, whereas using (25) requires only N^2. Since $\mathbf{F}_j$ is a function of $\mathbf{W}_j$ and $\nabla\mathbf{W}_j$, the evaluation of $\mathbf{F}_j$ is an expensive operation compared with averaging and so it is cheaper to use the methodology adopted here. This approach is also preferred because of the additional smoothness of $\mathbf{f}$ compared with $\mathbf{w}$ in the neighbourhood of shocks.

The integration rule adopted here results in a nine-point stencil for the advective terms, as does the method of Hall.[1] Other workers[14,16] have adopted the vertex-centred approach but only use a five-point stencil, which is less accurate on distorted meshes.

2.2. Evaluation of the viscous terms

In order to evaluate the viscous fluxes (6), $\nabla\mathbf{W}_j$ is required at the vertices $\mathbf{x}_j$ of the primary mesh. This is approximated by means of the finite volume technique adopted above. Suppose ϕ is some continuous scalar quantity defined over Ω and approximated at the vertices $\mathbf{x}_j$ by Φ_j. then $\nabla\Phi_j$ may be obtained from

$$\nabla\Phi_j \approx \frac{1}{V_j}\oint_{\delta\Omega_j} \phi\mathbf{n}\, ds \tag{26}$$

and the integral in (26) may be evaluated in an analogous fashion to (14) using nodal values Φ_j.

The vector line integral along the southern line of primary cell α in Figure 3 is

$$l_{\alpha,S} = \Phi_S\mathbf{n}_{NS}S_{NS}, \tag{27}$$

where Φ_S is averaged as in equation (25). Line integrals $l_{\alpha,N}$, $l_{\alpha,E}$ and $l_{\alpha,W}$ are similarly defined. The contribution of the contour integral (26) from primary cell α to, say, vertex $\mathbf{x}_2$ in Figure 3 can be expressed as

$$c_{\alpha,2} = l_{\alpha,E} - l_{\alpha,S} \tag{28}$$

and similarly for $c_{\alpha,1}$ $c_{\alpha,3}$ and $c_{\alpha,4}$. In an analogous fashion to (16)

$$\nabla\Phi_j = \frac{1}{V_j}\sum_{\alpha=1}^{p} c_{\alpha,j} \tag{29}$$

for p primary cells with common vertex $\mathbf{x}_j$. Hence equation (29) can be used componentwise to evaluate $\nabla\mathbf{W}_j$.

This leads to a 25-point stencil for diffusion at an interior vertex surrounded by four primary cells. Although this may at first appear unwieldy, because the contour integrals in (16) and (29)

are formed by distributing information from primary cells, it is not complicated or expensive to construct the residual.

This discretization is consistent in the sense that the viscous and inviscid fluxes are balanced over the same control volume. In Reference 17 the viscous terms are balanced over the control volume adopted here; however, the inviscid balance is performed as in Reference 18 using the area-weighted cell vertex scheme first described in Reference 19.

One advantage of the current treatment of viscous terms is that only one integration rule is required to evaluate the discrete residual (16), which will require less overhead in geometrical storage; this is thought to be especially important in three dimensions.

2.3. *Artificial dissipation*

The discretization outlined above leads to a central-difference-type approximation for advection, which is renowned for its instability, and as mentioned above, the viscous discretization cannot be relied upon to stabilize the scheme, hence the need for artificial dissipation. The model used here is closely related to that of Reference 6, which in turn is an adaptation of the successful model attributed to Jameson *et al.*[9] This consists of a blend of second and fourth differences.

With reference to Figure 3, let δ_ξ^2 and δ_η^2 represent the undivided second-difference operators in the ξ- and η-mesh-alinged co-ordinate directions respectively. The dissipation model is added as a perturbation to the flux integral as in equation (24). Assuming the ξ-co-ordinate lies along the southern edge of cell α in Figure 3, then

$$\mathbf{D}_S = \tau^{(2,\xi)}(\mathbf{W}_1 - \mathbf{W}_2) - \tau^{(4,\xi)}(\delta_\xi^2 \mathbf{W}_1 - \delta_\xi^2 \mathbf{W}_2), \tag{30}$$

with

$$\tau^{(2,\xi)} := \varepsilon^{(2)} \max_{j \in P_j} \{\kappa_j^\xi\}, \tag{31}$$

$$\tau^{(4,\xi)} := \max\{0, \varepsilon^{(4)} - \tau^{(2,\xi)}\}, \tag{32}$$

where $\varepsilon^{(2)}$ and $\varepsilon^{(4)}$ are global constants, P_j represents the set of four adjacent primary vertices along the ξ-co-ordinate line centered on the southern edge and

$$\kappa_j^\xi = \frac{|\delta_\xi^2 p_j|}{(4 + \delta_\xi^2) p_j}. \tag{33}$$

Similarly κ_j^η and thus $\mathbf{D}_E$, $\mathbf{D}_W$ and $\mathbf{D}_N$ can be defined. The differences and coefficients in $\mathbf{D}_S$ are solely based along an edge and it is for notational purposes that they are associated with a primary cell. Clearly $\mathbf{D}_S$ will be identical with $\mathbf{D}_N$ for the cell whose northern edge is the southern edge of α, so the differences $\mathbf{D}$ are evaluated before the integrals (14).

These edge-based differences are scaled by a cell-based upwind factor λ_{NS} in equation (24). This is based on the largest eigenvalue of the inviscid Jacobians $A = \partial \mathbf{f}^I / \partial \mathbf{w}$ and $B = \partial \mathbf{g}^I / \partial \mathbf{w}$ rotated into a normal co-ordinate frame and integrated; thus

$$\lambda_{NS} = (|u_0, v_0) \cdot \mathbf{n}_{NS}| + c_0) S_{NS}. \tag{34}$$

These artificial diffusion terms are the integral of undivided differences around the control volume. In smooth areas of flow the dominant terms are $O(h^3)$ and so will not effect the expected second-order accuracy of the discretization. In regions where the second pressure differences κ_j^ξ, and κ_j^η become large, the resulting perturbation to the residual (16) is a second derivative of $\mathbf{W}$

scaled by an $O(h)$ quantity. This results in a first-order upwinded residual, ideal for capturing shocks. However, as will be apparent in Section 4, this is shown to be inadequate for the general case.

On the high-aspect ratio grids required to resolve turbulent boundary layers, where $\lambda_{NS}/\lambda_{EW} > 10^3$, the fourth-order dissipation terms will become highly anisotropic. This significantly reduces the stabilizing effect of the artificial dissipation and hence the speed of convergence of an iterative solver.[20] The technique adopted in Reference 21 is used to prevent this by redefining

$$\begin{pmatrix} \lambda_{NS} \\ \lambda_{EW} \end{pmatrix} := \begin{pmatrix} [\max(1, \lambda_{EW}/\lambda_{NS})]^{\chi} \lambda_{NS} \\ [\max(1, \lambda_{NS}/\lambda_{EW})]^{\chi} \lambda_{EW} \end{pmatrix}, \tag{35}$$

where $\chi = 3/4$. This limits any anisotropic effects caused by mesh stretching; the less drastic effect of mesh-aligned flow is also taken into account.

2.4. *Boundary conditions*

For a vertex $\mathbf{x}_j$ on the boundary of the primary mesh the control volume used is shown in Figure 4. This ensures that the unions of the primary mesh cells and control volumes are identical. The same volume is also used for evaluating the gradients $\nabla \mathbf{W}_j$.

2.4.1. Solid wall. On a solid wall a no-slip condition is imposed by setting all the components of momentum in the residual to zero. In addition, the normal component of the vector ∇T is disregarded for the evaluation of the heat fluxes (11) and (12). Thus

$$\nabla T := \begin{pmatrix} \hat{n}_2^2 & -\hat{n}_1\hat{n}_2 \\ -\hat{n}_1\hat{n}_2 & \hat{n}_1^2 \end{pmatrix} \nabla T, \tag{36}$$

where $\hat{\mathbf{n}} = (\hat{n}_1, \hat{n}_2)^{\mathrm{T}}$ is the unit inward normal to the domain at vertex $\mathbf{x}_j$. This corresponds to a weak prescription of the adiabatic condition $\partial T/\partial \hat{n} = 0$.

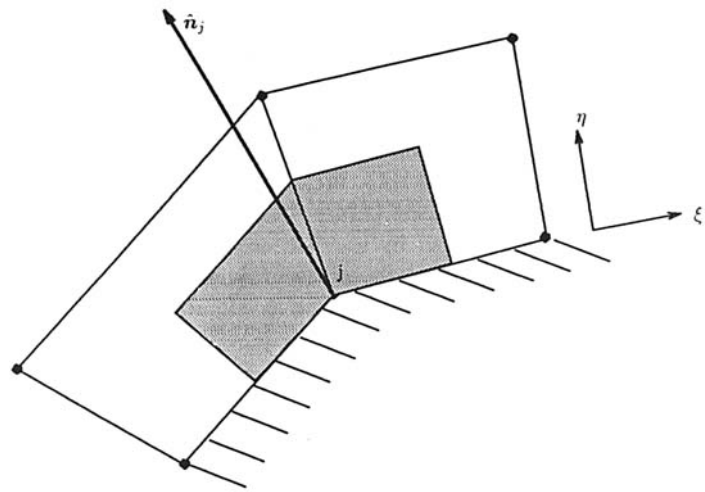

Figure 4. A control volume on the boundary; $\hat{\mathbf{n}}_j$ is the inward normnal at vertex $\mathbf{x}_j$

2.4.2. Free stream. On a freestream boundary the flow is assumed to be essentially inviscid and so the fluxes on the boundary are augmented to take account of incoming and outgoing inviscid characteristic information. A flux $\mathbf{F}_j$ on a freestream boundary is evaluated as

$$\mathbf{F}_j = \mathbf{f}(\tilde{\mathbf{W}}_j, \nabla \mathbf{W}_j), \tag{37}$$

where $\nabla \mathbf{W}_j$ is evaluated as in the interior. $\tilde{\mathbf{W}}_j$ is a non-linear combination of $\mathbf{W}_j$ and an infinity state derived from the vortex correction method described in Reference 22. This combination takes account of incoming and outgoing characteristic variables normal to the domain, also described in Reference 22. This treatment of freestream boundaries imposes no explicit condition on the solution $\mathbf{W}_j$. An implicit condition is imposed on the residual through the fluxes.

2.4.3. Artificial dissipation. On a freestream or wall boundary the dissipation terms in the boundary co-ordinate, labelled ξ in Figure 4, are unchanged from an internal node as in equation (30). However, in the η-co-ordinate or normal co-ordinate $\delta_\eta^2 \mathbf{W}_j$ is set to zero on the boundary, with all other terms evaluated as in the interior case. This condition approximately imposes $\partial^2 \mathbf{w}_j / \partial^2 \eta = 0$ and $\partial^3 \mathbf{w}_j / \partial^3 \eta = 0$ on the fourth difference normal to the wall. There is theoretical evidence in Reference 23 which suggests that these are the correct conditions to impose.

2.4.4. Internal. Since the discretization is a distribution of primary-cell-based quantities, it is trivial to accumulate the residual across any internal boundaries. However, for the artificial dissipation terms evaluated along each edge a simple accumulation is not sufficient to avoid excessive communication between blocks. At present the second differences δ_ξ^2 and δ_η^2 are explicitly calculated across any internal boundaries that may lie in the ξ- or η-direction. However, for a general multiblock mesh, where thousands of blocks may be needed to resolve the domain, it is envisaged that some approximation to the artificial diffusion terms may be necessary.

With the above prescriptions a system of residuals has been defined with boundary conditions implicitly imposed. This is a useful feature for the successful implementation of multigrid.

3. SOLUTION PROCEDURE

The solution procedure adopted here is a FAS multigrid method first introduced by Brandt[24] and successfully applied to the Euler equations in Reference 8. It uses a four-stage Runge–Kutta method as the smoothing procedure, a conservative area-weighted restriction and bilinear interpolation as the prolongation. This basic algorithm has been well documented in the literature.[8,25,26] For more general multigrid methods see Reference 27.

The following strategy was used in order to ensure robustness and efficiency:

(i) W-cycles with four or five pre- and post-smoothing iterations at every stage,
(ii) a full multigrid (FMG) start-up procedure,
(iii) overrelaxation of the Runge–Kutta time-stepping method with a Courant number of 2.6,
(iv) modification of the coarse grid operator as described below.

In Reference 28 the multigrid method is interpreted as an approximation cyclic reduction algorithm. This suggests that when solving advection–diffusion problems, the diffusion for the coarse grid operator should be increased for optimal convergence. This also seems sensible from a numerical viewpoint, since the coarse grids cannot resolve the boundary layer, which results

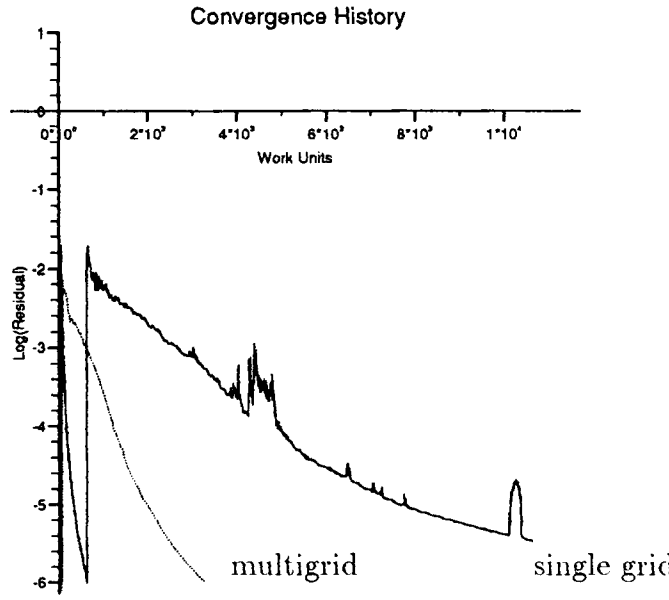

Figure 5. Plot of work done against residual reduction for single-and multigrid methods; RAE 2822 aerofoil test problem

in instability. In order to mimic the algorithm described in Reference 28, the technique adopted in Reference 6 is used by redefining κ_j^{ξ} on the coarse grid to be

$$\kappa_j^{\xi} = \max\left(\varepsilon_{\mathrm{H}}, \frac{|\delta_{\xi}^2 p_j|}{(4 + \delta_{\xi}^2)p_j}\right), \tag{38}$$

where κ_j^{η} is defined similarly and ε_{H} is a global constant. In addition, the anisotropic parameter χ in equation (35) is set to unity on coarse grids. Thus the maximum of λ_{NS} and λ_{EW} is used in each direction.

A comparison between multigrid and single-grid convergence is shown in Figure 5 for the turbulent transonic flow past an RAE 2822 aerofoil; $\log(\|\mathbf{R}\|_2)$ is plotted against work units. A work unit is the cost of a single Runge–Kutta iteration on the finest grid. The oscillations at the beginning of the curves in Figure 5 are due to the FMG start-up. For a fair comparison the single-grid iteration solved the coarse grid problem to get the same initial guess. Clearly a fivefold speed-up is observed, but more importantly the multigrid convergence history is less oscillatory. The single-grid oscillations are thought to be due to the turbulence model. At a stricter tolerance the benefit of multigrid over a single-grid method is expected to be more significant.

4. NORMAL SHOCK DETECTION

The procedure for capturing shocks outlined in Section 2.3 is based on adding a second-order diffusion operator in regions where the second difference in pressure becomes large. This is thought to be inadequate for transonic viscous calculations with shock-boundary layer interaction. The switch κ_j^{ξ} in equation (33) cannot distinguish between a shock and a large second pressure difference which may occur away from shocks in a boundary layer or indeed at the

leading edge of an aerofoil. In order to rectify this, a region of shocked flow is flagged before every Runge–Kutta time step. An alternative approach used in Reference 21 is to scale the pressure switches by the local Mach number. This is not as specific as the current approach where dissipation is only used in the shocked region. In the present work a robust and efficient technique has been developed for detecting this region where a normal shock lies. In accordance with the discretization philosophy, this is performed by flagging cells and so maintaining the flexibility of the algorithm to cope with geometrical difficulties.

The detection procedure is based on careful examination of the $M = 1$ contour. Firstly a vertex-based flag S_j is defined over the mesh:

$$S_j = \tfrac{1}{2}[1 - \operatorname{sgn}(1 - M_j)], \tag{39}$$

where M_j is the local Mach number at vertex $\mathbf{x}_j$. Thus $S_j = 1$ defines all the vertices with supersonic states. The $M = 1$ contour passes through a given cell Ω_j if

$$0 < \sum_{\mathbf{x}_i \in \Omega_j} S_i < 4, \tag{40}$$

and further processing is thus required. The states on either side of the $M = 1$ line within these cells are averaged as

$$\mathbf{U}_L = \frac{\sum_{\mathbf{x}_i \in \Omega_j} S_i \mathbf{U}_i}{\sum_{\mathbf{x}_i \in \Omega_j} S_i}, \qquad \mathbf{U}_R = \frac{\sum_{\mathbf{x}_i \in \Omega_j} (1 - S_i)\mathbf{U}_i}{4 - \sum_{\mathbf{x}_i \in \Omega_j} S_i}, \tag{41}$$

where $\mathbf{U}$ is the vector $(p, u, v, c)^T$, with a similar averaging for $\mathbf{x}_L$ and $\mathbf{x}_R$. then along every edge of these cells the Mach number is linearly interpolated to find two points $\mathbf{x}_A$ and $\mathbf{x}_B$ where $M = 1$ (see Figure 6). It is possible to find four points within a quadrilateral where $M = 1$, in which case the first two are chosen; this possibility never occurred in any converged results. The unit normal to this contour can be expressed as

$$\mathbf{n}_s = \frac{1}{|\delta \mathbf{x}_{AB}|} (-(y_A - y_B), (x_A - x_B))^T, \tag{42}$$

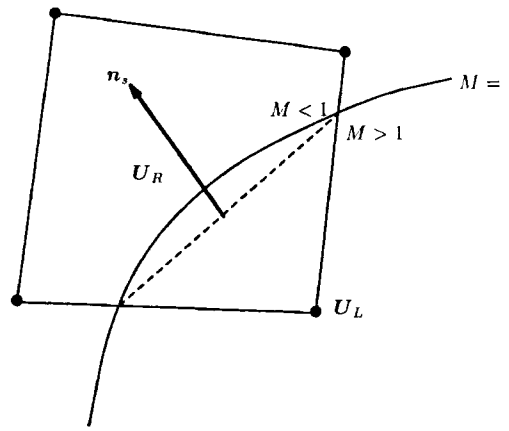

Figure 6. Shock detection procedure

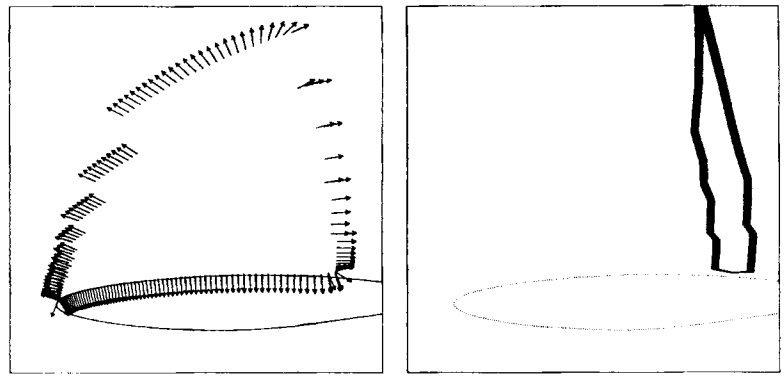

(a) (b)

Figure 7. (a) Vector plot of normals to $M = 1$ contour and (b) detected shock region for RAE 2822 test case

where $\delta \mathbf{x}_{NM} = \mathbf{x}_N - \mathbf{x}_M$. To ensure that $\mathbf{n}_s$ is always the outward normal to the supersonic region,

$$\mathbf{n}_s := \operatorname{sgn}(\delta \mathbf{x}_{RL} \cdot \mathbf{n}_s)\mathbf{n}_s. \tag{43}$$

A vector plot of these normals is illustrated in Figure 7(a) for a converged solution of turbulent transonic flow. It now remains to employ a simple test between $\mathbf{U}_L$ and $\mathbf{U}_R$ to differentiate between a shock and a sonic line. The cell-based switch S_α is defined as

$$S_\alpha = \tfrac{1}{4}\{\operatorname{sgn}[\mathbf{u}_0 \cdot \mathbf{n}_s(p_L - p_R)] + 1\}\{1 - \operatorname{sgn}[(M_R - 1)(M_L - 1)]\}, \tag{44}$$

where

$$M_L = \frac{|\mathbf{u}_L \cdot \mathbf{n}_s|}{c_L}, \qquad M_R = \frac{|\mathbf{u}_R \cdot \mathbf{n}_s|}{c_R} \tag{45}$$

and $\mathbf{u} = (u, v)^T$. The primary-cell-based switch S_α in (44) is zero away from the shock and unity if the shock passes through primary cell α. This switch is based on the jump in pressure normal to the $M = 1$ contour, in conjunction with the sign on the velocity through this contour. Since the shocks are still to be captured over perhaps four intervals, any primary cells within a two-cell radius of an $S_\alpha = 1$ cell are also flagged. This region is illustrated in Figure 7(b), which clearly shows where the shock and boundary layer meet. One of the advantages of this procedure is its robustness; only the shock is detected and the sonic line between the supersonic region and the boundary layer will never be flagged, since the Mach numbers resolved normal to the $M = 1$ contour will always be very much less than unity. This cannot be said of other detection procedures;[29,30] however, these methods can detect oblique shocks, which will not be found with the procedure adopted here.

To implement this algorithm, the edge-based shock-capturing coefficients κ_j^ξ and κ_j^η are scaled by the S_α for the neighbouring cells α. This ensures that second-order dissipation will only come into effect in the shocked region.

Although at first sight this test may appear expensive, after the initial test (40) has been performed over all primary cells, work is only required on a small subset of the domain, i.e. on the cells which contain the $M = 1$ contour. This detection procedure is only performed on the

finest grid, S_α being set to unity for all α on coarse grids. The computational overhead has been found to be negligible, as has the effect on the overall convergence history.

5. FOURIER ANALYSIS

For the vertex-centred methodology the control volume on a non-uniform mesh is not unique (see Figure 2). However, on a uniform mesh it is clear that the two approaches discussed lead to identical volumes. This section presents a Fourier analysis for two discretizations on a uniform mesh with step length h. Since this work is directed towards external aerodynamics problems, where the majority of the flow is essentially inviscid, linear advection is taken as the model problem, i.e.

$$\mathbf{a}\cdot\nabla u = 0, \tag{46}$$

where $\mathbf{a} = (a, b)^{\mathrm{T}}$ is some constant velocity field.

The advective discretization of Hall[1] averages states to the centroids and uses the trapezium quadrature rule around the control volume to obtain the nine-point stencil

$$\mathbf{a}\cdot\nabla u \approx \frac{1}{8h}\begin{bmatrix} -(a-b) & 2b & (a+b) \\ -2a & 0 & 2a \\ -(a+b) & -2b & (a-b) \end{bmatrix} U, \tag{47}$$

where U is an approximation to u. The Fourier symbol $S(\theta)$ is defined by

$$L\exp\left(\frac{i}{h}\boldsymbol{\theta}\cdot\mathbf{x}\right) = S(\boldsymbol{\theta})\exp\left(\frac{i}{h}\boldsymbol{\theta}\cdot\mathbf{x}\right), \quad \boldsymbol{\theta} = (\theta_1, \theta_2)^{\mathrm{T}} \in (-\pi, \pi]^2, \tag{48}$$

where L is the discrete operator and $\mathbf{x}$ are the co-ordinates of the mesh. For the discretization in equation (47) this is given by

$$S(\boldsymbol{\theta}) = \frac{i}{4h}\left[2a\sin\theta_1 + 2b\sin\theta_2 + (a+b)\sin(\theta_1+\theta_2) + (a-b)\sin(\theta_1-\theta_2)\right]. \tag{49}$$

This represents the effect of the operator (47) on the various Fourier modes in (48). Modes which lie in the null space of the operator, corresponding to $S(\theta) = 0$, are of particular interest. The multigrid procedure outlined in Section 3 is reliant on non-zero vlaues of this symbol for all high-frequency modes. The symbol vanishes not only at $\theta = (0, 0)^{\mathrm{T}}$, which is the consistency condition, but also at

$$\boldsymbol{\theta} = (\pi, \theta_2), (\theta_1, \pi). \tag{50}$$

Thus no high-frequency damping is obtained and hence this method is solely reliant on artificial dissipation.

The present discretization for advection uses a composite midpoint rule along each edge of the control volume, giving the nine-point stencil

$$\mathbf{a}\cdot\nabla u \approx \frac{1}{16h}\begin{bmatrix} -(a-b) & 6b & (a+b) \\ -6a & 0 & 6a \\ -(a+b) & -6b & (a-b) \end{bmatrix} U, \tag{51}$$

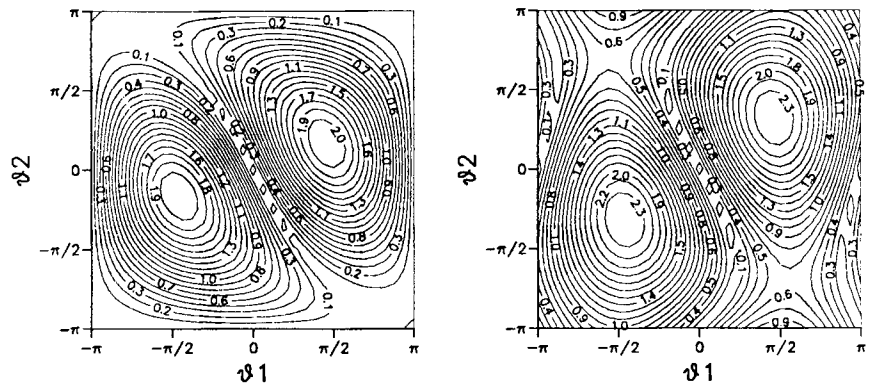

(a) (b)

Figure 8. Comparison of advective symbols of (a) Hall[1] and (b) present scheme

with symbol

$$S(\boldsymbol{\theta}) = \frac{i}{8h}\,[6a \sin\theta_1 + 6b \sin\theta_2 + (a+b)\sin(\theta_1+\theta_2) + (a-b)\sin(\theta_1-\theta_2)]. \tag{52}$$

The symbol vanishes for $\theta = (0, 0)^T$ and in addition for

$$\boldsymbol{\theta} = (\pi, 0), (0, \pi), (\pi, \pi). \tag{53}$$

In this case only the chequer-board and anisotropic modes lie in the null space.

Contour plots of the two symbols examined are presented in Figure 8 for $\mathbf{a} = (2, 1)$ which clearly illustrate the spectral advantages of the present scheme. However, artificial dissipation is still essential for the damping of the remaining modes.

The symbol of the present scheme has similar high-frequency damping to that of the five-point scheme in Reference 14. For the test problem in (46) this results in a simple central difference scheme which is not accurate on distoreted meshes and so is not discussed any further.

6. NUMERICAL RESULTS

In order to evaluate the accuracy of the algorithm, two widely documented test problems are examined in detail. The first is laminar flow past an NACA 0012 aerofoil at zero angle of attack ($\alpha = 0$), $Re = 5000$ and $M_\infty = 0.5$. The second is the more physical turbulent transonic flow past an RAE 2822 aerofoil at $\alpha = 2.79$, $M_\infty = 0.73$ and $Re = 6.5 \times 10^6$.

6.1. Laminar flow past an NACA 0012 aerofoil

This test case is ideal for the evaluation of the performance of the method since it is a laminar, totally subsonic, non-lifting case. Hence spurious effects due to turbulence modelling, shocks and far-field boundary conditions cannot pollute the solution. In addition, results for this test case are abundant in the literature (see Table II). Here mesh refinement and artificial dissipation studies are presented along with a budget balance of inviscid, viscous and artificial dissipation fluxes.

Table I. Details of NACA 0012 meshes; ΔS is the normal mesh spacing at the leading edge

Size	Points on aerofoil	ΔS	Far field
513 × 65	383	2×10^{-4}	10 chords
193 × 49	95	5×10^{-4}	10 chords
129 × 33	65	4×10^{-4}	10 chords

The three meshes used in the refinement study were also used in a similar study in Reference 3 and are outlined in Table I. Figure 9 and 10 shows details of the grid resolution at the leading and trailing edges of these meshes respectively. Clearly the 513 × 65 mesh is much finer than the other meshes and is used to give a baseline solution in order to assess the performance of the method on the remaining grids.

Figure 11 shows a detailed comparison of the skin friction coefficient C_f for the three meshes at the leading edge and the separation point, where C_f changes sign. Around the leading edge (Figure 11(a)) the comparison is good, whereas at the separation point (Figure 11(b)) the agreement is remarkable. This is especially true since the body-wise spacing of the 129 × 33 mesh at the separation point is poor. Figure 12 shows the normal and tangential velocity components resolved on a line normal to the aerofoil at 90% chord. This line clearly cuts through the recirculation region (Figure 12(a)) and is thus thought to be highly sensitive region. Again

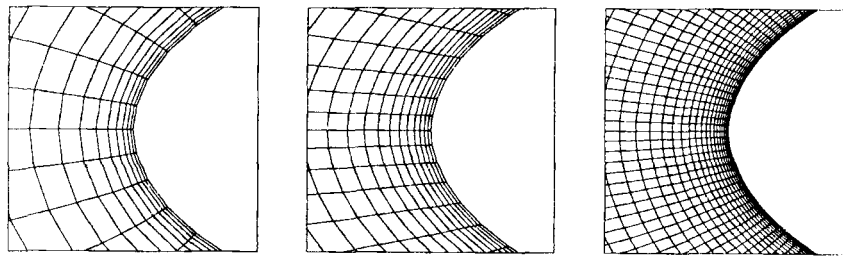

Figure 9. Primary mesh resolution at leading edge for NACA 0012: (a) 129 × 33; (b) 193 × 49; (c) 513 × 65

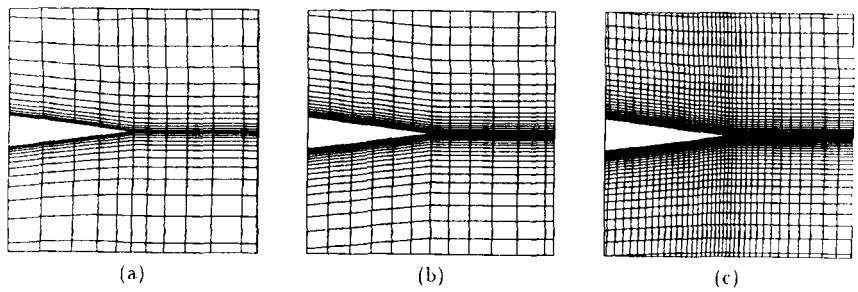

Figure 10. Mesh resolutin at trailing edge for NACA 0012: (a) 129 × 33; (b) 193 × 49; (c) 513 × 65

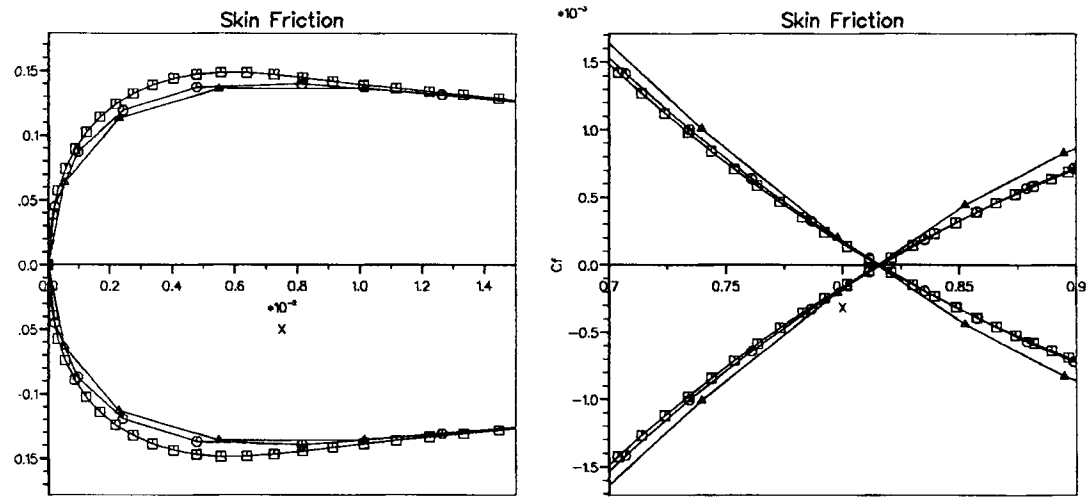

Figure 11. Skin friction coefficients at (a) leading edge and (b) separation point for NACA 0012 test case on meshes: △, 129 × 33; ○, 193 × 49; □, 513 × 65

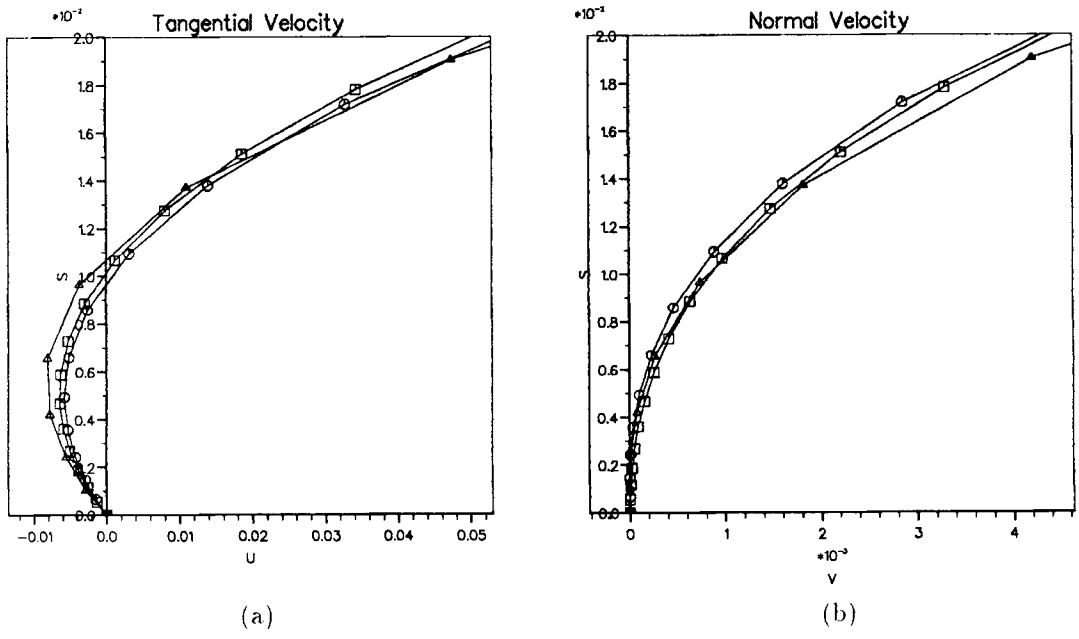

Figure 12. Interpolated (a) tangential and (b) normal velocity profiles at 95% chord through separated region for subsonic NACA 0012 test case on meshes: △, 129 × 33; ○, 193 × 49; □, 513 × 65

Table II. Comparison with other authors for NACA 0012 test case

Author	Grid	C_D^I	C_D^V	Separation point (% chord)
Present	513 × 65	0·0226	0·0328	81·5
Present	193 × 49	0·0224	0·0329	81·6
Present	129 × 33	0·0225	0·0328	81·3
Reference 5	513 × 65	0·0226	0·0328	81·9
Reference 5	193 × 49	0·0226	0·0326	81·9
Reference 5	129 × 33	0·0230	0·0322	80·6
Reference 7	320 × 64	0·0229	0·0332	81·4
Reference 31	320 × 64	0·0219	0·0337	81·9
Reference 25	512 × 128	0·0224	0·0330	81·4

good agreement is observed. Table II presents a comparison of the inviscid drag coefficient C_D^I and the viscous drag coefficient C_D^V for the three meshes and the results of other workers; good agreement is observed. These comparisons with the baseline solution illustrate that highly accurate solutions may be obtained on relatively coarse meshes using the current method.

Table III shows the dependence of the solution on $\varepsilon^{(4)}$, the global fourth-order artificial dissipation coefficient. This variance is acceptable, with little effect on the work units required to obtain these solutions to a fixed tolerance. For this test case, where the flow field is totally subsonic, the global constant $\varepsilon^{(2)}$ governing the shock-capturing dissipation is irrelevant, since the shock detection algorithm ensures that no second-order dissipation is added.

Figure 13 shows the x-momentum flux balance of the inviscid, viscous and artificial dissipation contributions to residuals in the boundary layer. Away from the aerofoil the viscous flux is essentially zero, so if these plots were extended to the freestream, a balance of inviscid and artificial dissipation terms would be observed. This is the case everywhere for a Euler calculation. It is for this reason that care must be taken in interpreting these plots. Clearly in Figure 13(a) the artificial dissipation terms are negligible near the wall. It is essentially only through the boundary layer edge that these fluxes become comparable with the physical terms. Figure 13(b) shows the same balance in the body co-ordinate at about 1% chord away from the aerofoil. At the leading edge $s = 0$ the flow is essentially inviscid and the boundary layer has not developed, so the viscous fluxes are negligible. Away from the leading edge the boundary layer has developed and the balance shows the artificial dissipation terms to be negligible. However, as in Figure 13(a), the artificial dissipation fluxes become apparent when passing from a viscous to an inviscid region. This behaviour is typical.

Table III. Effect of fourth-order dissipation for NACA 0012 test case

$\varepsilon^{(4)}$	C_D^I	C_D^I	Separation point (% chord)	Work units
1/64	0·0223	0·0334	82·0	3744
1/128	0·0224	0·0329	81·6	4359
1/256	0·0224	0·0326	81·4	4995

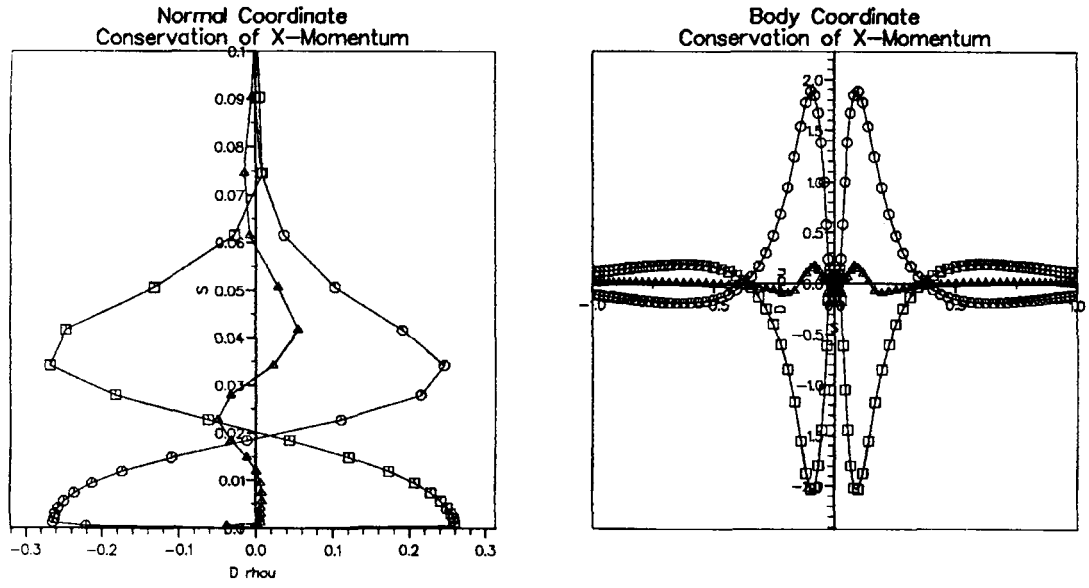

Figure 13. Equation budget of x-momentum of residual—□, inviscid; ○, viscous; △, artificial dissipation—for subsonic NACA0012 test case, 193 × 49 mesh, (a) through boundary layer at 50% chord and (b) 1% chord away from aerofoil

6.2. *Turbulent flow past an RAE 2822 aerofoil*

This test case is again well documented in the literature and is chosen to illustrate the capability of the method applied to a physically realistic problem and to demonstrate the shock detection algorithm. The two meshes GRID 1 and GRID 5 used are summarized in Table IV. These were used as part of the European validation exercise EUROVAL.[32] GRID 1 is thought to be of poor quality in comparison with GRID 5, with too few points in the inviscid region. Both grids have similar near-wall resolution. Figure 14 shows in some detail the leading edge grid spacing. The normal to the wall co-ordinate was scaled by a factor of 15 to enable individual cells on the body to be observed (Figure 14(b)). It is in this region that aspect ratios are greater than 1000 and with the high curvature the phenomenon illustrated in Figure 2 occurs. Table V presents a comparison of lift and drag coefficient between the two grids used here and the results of other workers. Very good agreement is observed for the viscous drag C_D^V, but there is considerable spread in the inviscid drag C_D^I and the lift coefficient C_L.

Of particular interest is the effect of the shock detection algorithm on the solution. Clearly

Table IV. Details of RAE 2822 meshes; ΔS is the normal mesh spacing at the leading edge

Name	Size	Points on aerofoil	ΔS	Far field
GRID 1	256 × 64	207	4×10^{-6}	10 chords
GRID 5	272 × 96	207	4×10^{-6}	30 chords

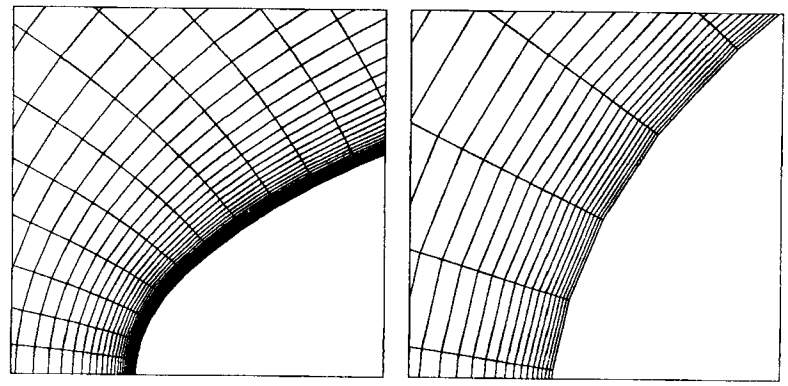

Figure 14. (a) View of RAE 2822 (257 × 65) mesh around leading edge. (b) A closer view with the normal to the wall co-ordinate scaled by 15

Table V. Comparison with other authors for RAE 2822 test case; SD denotes with shock detection

Author	Grid	C_L	C_D^I	C_D^V	C_D
Present	273 × 97	0·865	0·0131	0·0056	0·0199
Present + SD	273 × 97	0·875	0·0133	0·0058	0·0190
Present	256 × 65	0·844	0·0143	0·0055	0·0198
Present + SD	256 × 65	0·870	0·0132	0·0056	0·0188
Reference 6	256 × 65	0·848	0·0141	0·0053	0·0194
Reference 12	256 × 65	0·842	0·0121	0·0055	0·0175
Reference 33	256 × 65	0·829	0·0124	0·0051	0·0175
Reference 34	248 × 51	0·824	0·0128	0·0050	0·0178
Reference 32	273 × 97	0·837	0·0111	0·0056	0·0167

from Table V the most significant effect is on the lift coefficient C_L. Figure 15 shows plots of pressure coefficient and skin friction coefficient on the upper and lower surfaces in the shocked region for the two grids. A clear improvement is observed, with the shock detection algorithm giving almost grid-independent results. Without the shock detection the second-order dissipation is smearing the steep layers within the boundary layer; this is totally unphysical.

The results presented here give almost as accurate answers as the cell vertex results in Reference 5; this, in combination with the greater robustness of the scheme, makes this approach a worthwhile alternative. The authors believe that there is a strong argument for further development of both types of scheme.

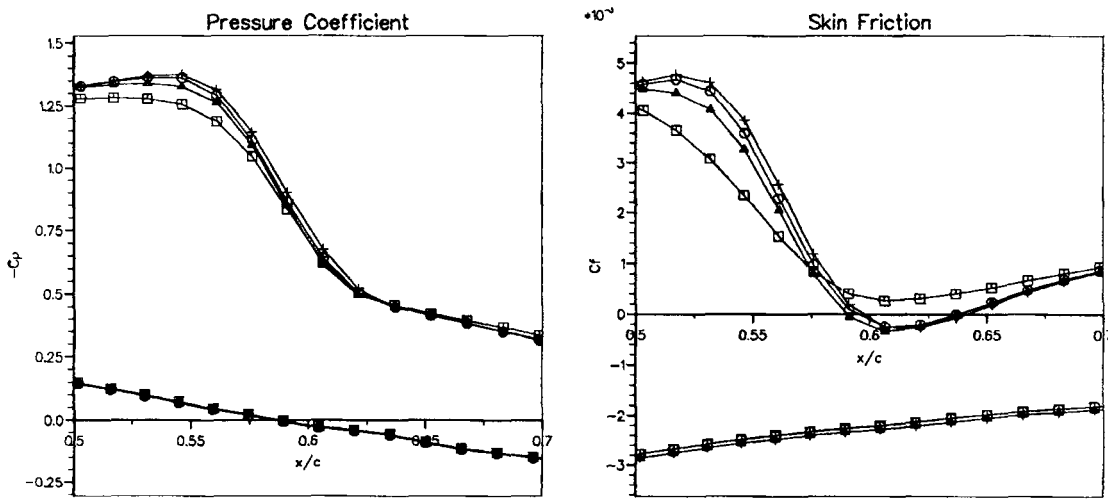

Figure 15. Comparison of (a) pressure coefficient and (b) skin friction around shocked region for RAE 2822 test case: □, 257 × 65; ○, 257 × 65 with shock detection; △, 273 × 97; +, 273 × 97 with shock detection

7. CONCLUSIONS

A consistent vertex-centred finite volume method has been presented which coped with the highly stretched and curved meshes required to resolve turbulent boundary layers around the leading edge of an aerofoil. In addition, the discretization will readily extend to general multiblock meshes in two and three dimensions.

Accurate answers were obtained on coarse meshes for both laminar and turbulent flow, the latter being achieved by the application of robust and efficient shock detection procedure which limits the areas where shock-capturing dissipation is applied.

ACKNOWLEDGEMENTS

This work was partly financed by BAe and SERC.

REFERENCES

1. M. G. Hall, 'A vertex centroid scheme for improved finite volume solution of the Navier–Stokes equations,' *AIAA Paper 91-1540*, 1991.
2. E. Dick, 'A flux-difference splitting method for steady Euler equations,' *J. Comput. Phys.* **76**, 19–32 (1988).
3. K. W. Morton, 'Finite volume methods and their analysis,' in J. R. Whiteman (ed.), *The Mathematics of Finite Elements and Applications VII MAFELAP 1990*, Academic, New York, 1991, pp. 189–214.
4. K. W. Morton, M. A. Rudgyard and G. J. Shaw, 'Upwind iteration methods for the cell vertex scheme in one dimension,' *Tech. rep. NA91/09*, Oxford University Computing Laboratory, 1991; submitted for publication.
5. K. W. Morton, P. I. Crumpton and J. A. Mackenzie, 'Cell vertex methods for inviscid and viscous flows,' *Comput Fluids*, Vol. 22, No 213, pp 91–102, 1993.
6. P. I. Crumpton, J. A. Mackenzie and K. W. Morton, 'Cell vertex algorithms for the compressible Navier–Stokes equations,' *Tech. Rep. NA91/12*, Oxford University Computing Laboratory, 1991; *Journal of Comp. Physics*, **109** (1), (1993).
7. D. J. Mavriplis, A. Jameson and L. Martinelli 'Multigrid solution of the Navier–Stokes equations on triangular meshes,' *AIAA Paper 89-0120*, 1989.

8. A. Jameson, 'Solution of the Euler equations by a multigrid method,' *Appl. Math. Comput.* **13**, 327–356 (1983).
9. A. Jameson, W. Schmidt and E. Turkel, 'Numerical solutions of the Euler equations by finite volume methods using Runge–Kutta time stepping,' *AIAA Paper 81-1259*, 1981.
10. H. Schlichting, *Boundary-layer theory*, McGraw-Hill, New York, 1955.
11. B. S. Baldwin and H. Lomax, 'Thin layer approximation and algebraic model for separated turbulent flows,' *AIAA Paper* 78–257, 1978.
12. R. Radespiel and C. Rossow, 'A cell vertex finite volume scheme for the two-dimensional Navier–Stokes equation.'
13. P. D. Lax and B. Wendroff, 'Systems of conservation laws,' *Commun. Pure Appl. Math.* **13**, 217–237 (1960).
14. K. Kroll and C. Rossow, 'A high resolution cell-vertex TVD scheme for the solution of the two and three dimensional euler equations,' in K. W. Morton (ed.), *Proc. Twelfth Int. Conf. on Numerical Methods in Fluid Dynamics*, Springer, Berlin, 1990, pp. 442–445.
15. N. P. Weatherill and C. R. Forsey, 'Grid generation and flow calculations for aircraft geometries,' *J. Aircraft*, **22**, 855–860 (1985).
16. J. W. Van Der Burg and J. G. M. Kierten, 'Improved shock-capturing of Jameson's scheme for the Euler equations,' *Tech. Rep. Memo. No. 997*, Faculty of Applied Mathematics, University of Twente, 1991.
17. F. Liu and A. Jameson, 'Cascade flow calculation by a multigrid vertex scheme for the Navier–Stokes equations,' in K. W. Morton (ed.). *Proc. Fourth Int. Symp. on Computational Fluid Dynamics*, Vol. II, ICASE, 1991, pp. 699–704.
18. A. Jameson and T. J. Baker, 'Solution of the Euler equations for complex configurations,' *AIAA Paper 83-1929*, 1983.
19. M. G. Hall. 'Cell-vertex multigrid schemes of the Euler equations,' in K. W. Morton and M. J. Baines (eds), *Proc. Conf. on Numerical Methods for Fluid Dynamics*, Oxford University Press, Oxford, 1985, pp. 303–345.
20. K. Stuben and U. Trottenberg, 'Multigrid methods: fundamental algorithms, model problem analysis and applications,' in W. Hackbusch and U. Trottenberg (eds), *Lecture Notes in Mathematics*, Vol. 960, Springer, Berlin, 1982, pp. 1–176.
21. R. C. Swanson and E. Turkel, 'Artificial dissipation and central difference schemes for the Euler and Navier–Stokes equations,' *AIAA Paper 87-1107*, 1987, pp. 55–69.
22. J. L. Thomas and M. D. Salas, 'Far-field boundary conditions for transonic lifting solutions to the Euler equations,' *AIAA J.*, **24**, 1074–1080 (1986).
23. G. J. Shaw and P. I. Crumpton, 'An investigation of fourth order artificial diffusion,' *Tech. Rep.*, Oxford University Computing Laboratory, 199X.
24. A. Brandt, 'Multi-level adaptive solutions to boundary value problems,' *Math. Comput.* **31**, 333–390 (1977).
25. R. Radespiel and R. C. Swanson, 'An investigation of cell centered and cell vertex multigrid schemes for the Navier–Stokes equations,' *AIAA Paper 89-0548*, 1989.
26. R. V. Cima, E. Turkel and S. Schaffer, 'Comparison of three explicit multigrid methods for the Euler and Navier–Stokes equations,' *Tech. Memo. 88878, NASA ICOMP-86-3*, 1986.
27. P. Wesseling, *An Introduction to Multigrid Methods*, Wiley, Chichester, 1992.
28. G. J. Shaw and P. I. Crumpton, 'On the relationship between multigrid methods and cyclic reduction,' *Tech. Rep.*, Oxford University Computing Laboratory, 1990.
29. K. W. Morton and M. A. Rudgyard, 'Shock recovery and the cell vertex scheme for the steady Euler equations,' in D. L. Dwoyer, M. Y. Hussaini and R. G. Voigt (eds), *Lecture Notes in Physics*, Vol. 323, *Proc. 11th Int. Conf. on Numerical Methods in Fluid Dynamics*, Springer, Berlin, 1989, pp. 424–428.
30. K. W. Morton and M. F. Paisley, 'A finite volume scheme with shock fitting for the steady Euler equations,' *J Comput. Phys.*, **80**, 168–203 (1989).
31. L. Martinelli, 'Calculations of viscous flows with a multigrid method,' *Ph.D. Thesis*, Department of Mechanical and Aerospace Engineering, Princeton University, 1987.
32. J. J. Benton, 'Validation of 2d Navier–Stokes codes for aerofoils,' *Tech. rep. BRITE/EURAM 1066*, British Aerospace Research Department, Woodford, 1991.
33. R. C. Swanson and E. Turkel, 'A multistage time-stepping scheme for the Navier–Stokes equations,' *AIAA Paper 85-0035*, 1985.
34. T. H. Pulliam and J. L. Steger, 'Recent improvements in efficiency, accuracy and convergence for implicit approximate factorization algorithms,' *AIAA Paper 86-0274*, 1986.